Al-Azhar Bull. Sci. Vol. 19, No. 2 (Dec.): pp. 49-64, 2008.

ENCAPSULATION OF NICKEL(II)-SCHIFF BASE COMPLEX IN Y-ZEOLITE FOR *IN SITU* CHEMISORPTION OF CARBON MONOXIDE

TAREK M. SALAMA

Faculty of Science, Chemistry Department, Al-Azhar University, Nasr City 11884, Cairo, Egypt

Abstract

Encapsulation of nickel(II) complex of the Schiff base-type ligand (salicylidene-*p*-aminobenzoic acid) in the intracrysatalline nano-pores of zeolite-Y is reported. The zeolite-encapsulated trinuclear Ni(II)-Schiff base complex was prepared by diffusion of the ligand through pores of the zeolite, already exchanged with the respective metal (flexible ligand method). The host/guest compound obtained was characterized by elemental analysis, spectroscopic (IR and electronic) studies, surface texture, thermal analysis and powder x-ray diffraction (XRD). The solids were subjected to *in situ* FT-IR study of adsorbed carbon monoxide. IR and UV-vis as well as XRD data indicate that the chemical stoichiometry of the complex remains intact upon encapsulation and the geometric environment around the metal ions is a distorted tetrahedral. Experimental evidence indicates that the chemisorption of carbon monoxide is indeed catalyzed by the zeolite-encapsulated complex. Sorption of CO results in the appearance of a series of surface carbonyl species: linear Ni^{II}-CO (2198 cm^{-1}), bridged CO (1896 cm^{-1}), C=O derived from acetone-like species (1728 and 1686 cm^{-1}) and physisorbed CO_2 (2351 cm^{-1}). The acetone-like species are stable upon evacuation which can be considered as bound to Lewis acid sites in the zeolite Y. These species are most significant on the zeolite-encapsulated complex than on metal-exchanged zeolite.

***Keywords**:* NaY Zeolite; Encapsulation; Nickel complexes; *In situ* FTIR

Introduction

Zeolites are microporous aluminosilicates, whose structures characterize channels and cavities of strictly regular dimensions [1–2]. The well-defined and -ordered structure of zeolites provides an ideal environment to entrap active metal complexes or metal clusters, and such confinement leads to higher thermal stability by reducing dimerization of active sites [3-4]. A complex molecule encapsulated in zeolite cages is characterized by isolation from the other molecules by zeolite lattice and low mobility. Furthermore, if the size of the encapsulated complex molecule is hug enough in comparable to the zeolite cage, the molecule may suffer a strong steric restriction in the cage result in a distortion by confirmation of a new structure. In such a case the molecule in the cage may show interesting properties, which are not seen under ordinary conditions. Upon incorporation, the guest molecules are confined in the restricted space provided by the rigid framework of the zeolite and only interact with those reactant molecules being in close proximity. Thus,

incorporation of complexes inside zeolites makes it possible to perform catalytic reactions combining the advantages of homogeneous and heterogeneous catalytic systems with great importance due to their numerous industrial applications [5].

Metal complexes of porphyrins, phthalocyanines, Schiff-bases, etc. have been encapsulated into zeolitic matrix for the development of efficient biomimetic oxidation catalysts which have acted as the functional mimic of metalloenzymes [6-7]. Owing to the large size (e.g. 10-14 Å) of these complexes in comparison to the free apertures diameter for the channels in case of NaY zeolite (7.4 Å), they can not be prepared through the condensation of metal complex molecules within the porous structures of zeolite. An alternative technique, the encapsulation of metal complexes in NaY by the flexible ligand method via ensembling step-wise ligand entities into the metal-exchanged zeolite and subsequent complexation, as has been recently reported [8]. Metal complexes have also been encapsulated by the synthesis of the zeolite in the presence of the preformed metal complexes (the so called 'zeolite synthesis' method) [9].

The early work on zeolite complexes was mainly restricted to mono- and binuclear-based complexes [10,11]. However, polynuclear systems with definable structure in zeolite cavities have not been well explored. We report here the encapsulation of trinuclear nickel complex of salicylidene-*p*-aminobenzoic (SPAB) using the flexible ligand (FL) method. Nickel(II) Schiff-base complexes are currently of considerable interest to promote oxidation reactions [12]. The routes for the formation of the complex are followed by UV–vis and FTIR spectroscopy. Besides, the texture of these composite materials is described to provide evidence for the successful occlusion of the metal complex within the zeolite matrix. Attempts have been made to correlate the structure-activity of the encapsulated Schiff-base complex and Ni(II) ions exchanged into zeolite. For this purpose, *in situ* FT-IR investigation of carbon monoxide sorption and subsequent reaction with residual water molecules in zeolite, i.e. basically a water-gas shift reaction [13], under low thermal activation was presented.

Experimental

Materials

All the chemicals used were of BDH or Analar grade quality. The sodium form of Y zeolite (HSZ-320N-NAA, Si/Al = 5.6, BET surface area = 910 m^2/g) obtained

from Toyota Company Ltd., Japan was dried at 300 °C for 4 h prior to being used as the host material for encapsulating complex.

Ligand synthesis

The salicylidene-*p*-aminobenzoic ligand (SPAB) was prepared, following the same procedure lined earlier in literatures (14,15), by condensing of salicyaldehyde with of the *p*-aminobenzoic acid (1/1 molar ratio) in absolute ethanol. The mixture was stirred under reflux for 1/2 h by which the solid obtained was filtered and crystallized from hot ethanol, dried at 110 °C for 24 h to produce yellow shiny crystals. The solid formed in this synthesis melts at 264-268 °C and was soluble in alcohol, chloroform, methylene chloride and acetone. The purity of the SPAB was firstly checked by the melting point constancy, elemental analyses and finally spectral methods; analysis found: C, 69.99; H, 4.20; N, 5.83%, cal. for $C_{14}H_{10}NO_3$ (SPAB), C, 69.90; H, 4.17; N, 5.81%. The mass spectrum of the free ligand showed a molecular ion peak at m/z 241 (M^+; 100%), cal. 240.23 [16].

Ion-exchanged zeolite

The NaY zeolite was ion-exchanged with Ni^{II} ions by the conventional procedure. 7.0 g of NaY zeolite was treated with 1500 m1 of 0.01M aqueous solution of nickel acetate tetrahydrate ($Ni(CH_3COO)_2$. $4H_2O$) at pH 5-6. The ion-exchange reaction was conducted at 80 °C for 24 h with continuous stirring. The solid was filtered off, washed thoroughly with distilled water till the washing solution was essentially free of Ni^{II} ions. The Ni^{II}-exchanged Y zeolite was then dried at 110 °C, calcined in air at 400 °C, and finally stored in desiccator until required for use (referred to as Ni^{II}/Y)

Encapsulated complex synthesis by the FL method

1.0 g of Ni^{II}/Y was degassed in a Schlenk tube (Pyrex glass) at 300 °C for 2 h, and then cooled down to room temperature. Part of the dried Ni^{II}/Y was then intimately mixed with an excess SPAB (2.0 g) in a glove bag filled with nitrogen atmosphere. The physically mixed precursor was placed horizontally in a Schlenk furnace tube, evacuated for 10 min (~10^{-4} Torr) before being heated with constant stirring to 150 °C for 24 h. The encapsulated solid obtained was washed with acetone, ethanol, methylene chloride and finally submitted to Soxhlet extraction with ethanol for 48 h at normal conditions to eliminate excess unreacted ligand and surface adsorbed complex. The encapsulated complex is designated as $Ni^{II}L/Y$ (L:

ligand). The formula, color and analytical data of Ni^{II}/Y and Ni^{II}L/Y are presented in Table 1 for comparison.

Physical methods and analysis

UV-Vis spectra were recorded in Nujol using Perkin-Elmer lambda 35 UV/Vis spectrophotometer. IR spectra were recorded as KBr pellet on a Mattson 5000 FT-IR spectrometer. Elemental analysis for carbon and hydrogen was determined at the Microanalytical Unit of Cairo University, Egypt. The mass susceptibility of solid materials was measured on magnetic susceptibility balance of models Johnson Metthey and Sherwood. X-ray diffraction (XRD) patterns of the samples were recorded using a Philips PW 1840 diffractometer with Cu Kα radiation (λ=1.54 Å). Thermal analyses (TG, DTG, and DTA) were carried out with a Shimadzu thermal analyzer model 50 H. The metal content was determined in the presence of some interfering aluminum ions by complexometric titration with EDTA using sodium fluoride (i.e. F^-) as a masking agent, xylenol orange as indicator and haxamine as a buffer [17].

The surface texture characteristics were obtained from nitrogen adsorption isotherms (at p/p_o = 0.95) at -196 $^\circ$C using a conventional home made volumetric apparatus. The specific surface area was calculated using the BET method. The samples were thermally degassed at 200 $^\circ$C prior to the adsorption measurements. The micropore volume and the external surface area were obtained from the t-plot method. FT-IR spectra of CO adsorbed on solids were recorded by use of an FT-IR instrument Bruker (Vector 22) single beam spectrometer with a resolution of 2 cm^{-1}. A self-supporting wafer of about 30 mg/cm^2 was placed in an in situ FT-IR quartz cell equipped with $CaCl_2$ windows and a built-in furnace. As a typical experiment the sample was thermally treated at 300 $^\circ$C for 1 h under a reduced pressure of 10^{-5} Torr prior to admitting CO (50 Torr) gas at room temperature. The spectra were subtracted from the background to evaluate the spectral changes due to CO adsorption.

Results and discussion

IR spectroscopy

The IR absorption bands of SPAB (free ligand), Ni^{II}-Y, Ni^{II}L/Y and parent NaY are listed in Table 2. The framework infrared spectrum of NaY is in agreement with previous data [18]. The absorption bands around 1032 (ν_{as}), 720 (ν_s) and 463 cm^{-1} (T–O bend) are three lattice modes associated with internal vibrations of the

$(Si,Al)O_4$ tetrahedra unites which designated as TO_4 in the framework of Y zeolite and are structure-insensitive. The structure-sensitive vibrations due to external linkages between tetrahedra are found at 1140 (ν_{as}), 787 (ν_s) and 576 cm^{-1} (double 6-rings) (Table 2). The domination of IR bands of zeolite Y matrix in the spectrum of Ni^{II}/Y gave rise to the structural integrity of the zeolite upon ion exchange. Consequently, no dealumination or a molecular distortion of initial tetrahedral symmetry of Y-zeolite took place as the zeolite structure-sensitive bands did not show any significant shift or broadening. This may suggest that the Ni^{II} ions react less drastically with the oxygen lattice of Y zeolite, thereby inhibiting partial destruction of the zeolite structure.

The strong new band observed at 1400 cm^{-1} in the spectra of Ni^{II}/Y attributed to δOH (in-plane) of H_2O molecules [19] indicates that the Ni^{II} ions are in coordination with water molecules, i.e. $[Ni(H_2O)_6]^{2+}$, inside the Y zeolite. The weakness of this band upon complexation indicates that the chelating ligand formed on the isolated metal ions species by replacement some of water molecules. A band appearing at ca. 1600 cm^{-1} in IR spectrum of SBAP can be assigned as the characteristic band for azomethine ν(C=N) stretch [20]. This band shifts to lower wave number for Ni^{II}L/Y compared to that of free ligand, i.e. 1542 cm^{-1}, indicating the involvement of azomethine nitrogen in coordination [21]. A similar shift for carborxylate groups of ligand coordinated to the electron withdrawing Ni^{II} ions upon complexation was observable, i.e. from 1686 to 1510 cm^{-1} [22]. Accordingly, the IR data supports the encapsulation of the complex in the zeolite matrix.

Electronic spectra and magnetic properties

The UV-Vis electronic spectra of the SBAP, Ni^{II}/Y and encapsulated complex are shown in Fig. 1, and the magnetic moment values are given in Table 1. The geometries are tentatively assigned for the encapsulated complex on the basis of adsorption bands and room temperature magnetic moment. The electronic spectrum of Ni^{II}/Y exhibits two prominent bands at 334 and 362 nm assigned to internal transactions of framework oxygen ligand (O^{2-}) to metal (Al^{III}) charge-transfer ($L \rightarrow M$) in Y zeolite [23]. The absence of these bands in the spectrum of Ni^{II}L/Y can be due to the complex moieties anchored onto the internal surface through M–O(zeolite) linkages. The magnetic moment value of 1.254 BM provides little information on the geometry for this sample (Table 1). The broad band around 507 nm in the spectrum of SBAP is due to ligand based electronic ($\pi \rightarrow \pi^*$) transition. However, this band is not present in the spectrum of Ni^{II}L/Y due to complex

formation. Balkus et al. [24] observed similar phenomenon in the cases of cobalt(II) and copper(II) perfurophathalocyanines encapsulated in Na-X zeolite; these were attributed to the distortion of the phthalocyanine ligand in the zeolite cage due to complex formation. The magnetic moment value of 2.365 BM for $Ni^{II}L/Y$ suggests a tetrahedral geometry around the Ni^{II} ions [25]. No d–d band(s) could be observed for $Ni^{II}L/Y$, possibly due to its poor loading.

X-ray diffraction (XRD)

Inspection of the X-ray diffractograms characterizes the parent to be pure NaY (Fig. 2(a)), which is found to be in good arrangement with the faujasite framework topology NaY [26]. The XRD patterns indicate that the crystallinity and morphology of NaY are preserved for the modified Ni^{II}/Y and $Ni^{II}L/Y$ samples (Fig. 2), in compatible with the IR results. Diffraction lines characteristic for any new phase were not detected in the diffractograms of the modified samples. A list of various samples investigated, with each one's unit cell parameter, cell volume and product crystallinity, is presented in Table 3. Least square analysis of the data in terms of a cubic lattice with unit cell parameter = 24.64 Å could be fitted for NaY. Changes in zeolite framework are deduced by comparing the unit cell parameter, calculated following the complex formation in zeolite Y, i.e. 24.49 Å, which showed a decrease (0.61 %) with that of the parent NaY. This suggests a slight shrinkage in the framework after encapsulation of complex.

It has been observed that empirical derived relationship exist between the relative 331, 311, and 220 peak intensities and cation location in faujasite type zeolites [27]. Cations are randomly distributed within the lattice if $I_{331} > I_{220} > I_{311}$, but if $I_{331} > I_{311} > I_{220}$, the cations assume positions at sites I^-, II. Using these empirical criteria, the diffraction patterns 2b and 2c suggest that the large $Ni^{II}L/Y$ complex is probably displaced Ni^{II} ions from their random positions within the NaY cavities to locations at sites I^-, II. Site I^- is reportedly located in the sodalite cavity while site II at the center of a single six-ring (S6R) or displaced from this point into a supercage [28].

Based on the results of elemental analysis listed in Table 1, IR, UV–Vis and XRD data of $Ni^{II}L/Y$, the flexible ligand synthesis imply the spatial configuration of the chelated groups around the central metal ions inside zeolite Y. A schematic diagram of the complex formation in supercage of zeolite is shown in Fig. 3.

Thermal analysis

The TG curve of Ni^{II}/Y showed four decomposition stages starting at 27, 96, 189 and 539 °C corresponding to the desorption of adsorbed water molecules from zeolite (Fig. 4). The DTA curve showed two peaks at 361 and 636 °C (Fig. 5). The first exothermic peak is attributed to the decomposition of supported acetate precursors while the second is an endothermic one. The latter peak is not accompanied by a weight loss, indicating a type of phase change. On the other hand, the TG curve of Ni^{II}L/Y showed two thermal stages corresponding to water loss at 35 °C and the second at 560 °C to decomposition of organic matter. The DTA curve of Ni^{II}L/Y showed only two endothermic peaks in the range 30-200 °C attributed to water loss from Y zeolite. In fact there is no any exothermic peak due to the decomposition of the encapsulated complex was observed in the DTA curve through the range of 30-1000 °C, suggesting the thermal of stability of this encapsulated complex up to 1000 °C.

Surface texture

The specific surface areas S_{BET} (m^2/g) of the prepared samples are determined using the BET equation, adopting a value of 16.2 $Å^2$ for the cross-sectional area of N_2 molecule according to the relation:

$$S_{BET} = n_m N \sigma / m$$

Where n_m is the number of moles of adsorbate (N_2) required to form a monolayer, N is the Avogadro number (6.022×10^{23} molecules /mole), σ is the cross-sectional area of N_2 molecule and m is the mass of adsorbent. The values of surface area (S_t) calculated from the $V_{l\text{-}t}$ plots were found to be comparable to the BET values (Table 3) indicating the proper choice of the t-curve.

An effective entrapment and integrity of the nickel complex inside the zeolite Y was also confirmed by measuring surface area and pore volume. Table 3 compares surface area, pore volume and sorption efficiencies of Ni^{II}L/Y with that of Ni^{II}/Y and pure NaY analogs. The observed difference in surface area and pore volume values for pure NaY and Ni^{II}L/Y indicate nearly 31-36 %, respectively, reduction due to the effective blockage by stabilized nickel complex in the zeolite Y pore structure. Since the zeolite framework structure is not affected by encapsulation as revealed by XRD, the large reduction of surface area and pore volume observed for the Ni-based zeolites is interpreted as arising from the presence of compounds in the zeolite cavities**.** A similar phenomenon was earlier observed on the encapsulation of

phthalocyanines [29]. The $Ni^{II}L/Y$ sample brought about a drastic decrease in the value of mean pore radius (r^-) as compared with that of NaY due to encapsulation of complex species into voids of zeolite Y. These results clearly provide direct evidence for the presence of nickel complex species which are intact inside the supercages of zeolite Y and not on the external surface. This is well supported by results on UV-vis, XRD and FTIR.

Adsorption of CO: IR spectroscopy

In situ FTIR technique was used to investigate the interaction of CO with the modified zeolite samples. This technique is widely employed for analysis of active sites on different materials because its ability to act as a weak σ-donor and π-acceptor, its sensitivity toward electrostatic fields surrounding metal cations, and its ability to interact with Lewis acid sites. Fig. 6 shows the IR spectra in the C–O stretching region of CO adsorbed at room temperature on the Ni^{II}/Y and $Ni^{II}L/Y$ samples previously outgassed in vacuo at 300 °C. Exposure to CO produced vibrational spectra with up to five infrared bands centered at 2351, 2198, 1896, 1728 and 1686 cm^{-1}. The band at 2351 cm^{-1} in the spectra of both samples can be ascribed to the ν_3 vibration of adsorbed CO_2, bound to the cation by ion-induced dipole interactions. This band therefore is a good indicator of CO_2 formation during the adsorption of CO over Ni^{II}/Y and $Ni^{II}L/Y$ samples which might be produced from interaction of CO and residual of H_2O molecules in the zeolite by the water–gas shift reaction (WGSR, $CO + H_2O \rightarrow CO_2 + H_2$). The absorption band at 2198 cm^{-1} is assigned to linear Ni^{II}-CO adducts according to data reported in the literature [30]. The initiated peak by CO coverage near 1896 cm^{-1}, emerges in the region of bridge CO adspecies [31]; or alternatively can be assigned to nickel carbonyl hydride species [32]. Thus carbonyl hydride species on nickel may form when $CO + H_2$ mixture interacts with a nickel catalyst. The hydrogen is produced via the low temperature WGSR. New sharp bands are found at 1728 and 1686 cm^{-1} $\nu_{as}(C=O)$, associated with adsorbed acetone vapor [33]. Acetone may be produced due to dynamic process of CO hydrogenation under reaction conditions. These bands are most prominent for $Ni^{II}L/Y$ than for Ni^{II}/Y. In the used synthesis reaction conditions, it is believed that the encapsulated complex in voids of zeolite Y undergoes some molecular distortion and this could potentially provide a way to effectively stabilize complex in the zeolite. It has been pointed out [34] that such distortions lead to a lower electron density on the metal ions by exhibiting a reduced potential for π* back-bonding ($d \rightarrow \pi^*$) and thus can enhance reactivity of the complex towards CO.

It is relevant to add that evacuation at room temperature led to disappearance of weakly bound carbonyl (CO) species at 2198 cm^{-1}, corresponding to Ni^{II}-CO adducts, whereas the other bands at 1896, 1728 and 1686 cm^{-1} were found to be very persistent. Subsequent rise in evacuation temperature to 50 °C makes little decrement in intensity of the latter bands. This implies high stability of the carbonyls derived from adsorbed organic species especially on the encapsulated complex plausibly due to association with Lewis acid sites in zeolite.

Summary and Conclusions

Schiff base complex of Nickel(II) has been encapsulated in the supercages of zeolite Y by introducing nickel into the NaY zeolite by ion exchange with diluted aqueous solution of $Ni(CH_3COO)_2.4H_2O$, followed by calcination in air at 400°C to decompose the acetate precursors. The nickel-metal-containing zeolite was mixed with an excess of the Schiff base ligand (n_{ligand}/n_{metal} = 4) in a glove box under nitrogen atmosphere, heated at 150 °C *in vacuo*, followed by an isothermal period of 24 h. The resulting composite material has been characterized by spectroscopic IR and UV-vis, XRD, elemental and thermal analyses, and adsorption techniques. An effective entrapment and integrity of the complex species encaged in zeolite Y was attained as $Ni^{II}L$ moieties were anchored onto the internal surface through M–O(zeolite) linkages. The encapsulated complex would appear to be more stable towards thermal dissociation. $Ni^{II}L/Y$ is reasonably good catalyst for the chemisorption of CO. The catalytic behavior could be mainly attributed to the state of nickel centers in the encapsulated complex by suggested enhancement of electron density induced on the metal to result in an increased CO adsorption activity. This in turn will be an urgent target for environmentally attractive processes.

Table 1. Chemical composition, physical and magnetic data of SPAB and modified zeolites.

Sample label	Color	M (wt.%)	M.p*./Decom p.p.°C	M/C ratio Found(calcd.)	$\mu_{eff/BM}$	Product assignment
SPAB	Yellow		264 - 268*			$C_{14}H_{10}NO_3$
Ni^{II}/Y	Pale green	5.90	> 300		1.254	$[Ni(H_2O)_6]^{2+}/Y$
$Ni^{II}L/Y$	yellowish	5.03	> 300	0.429(0.215)	2.356	$[Ni_3(SPAB)((H_2O)_8]^{4+}/Y$

Table 2. Significant IR bands of SPAB, NaY and modified zeolites.

Sample	Internal vibrations			External vibrations				Adsorbed	δ (OH)	ν(C=N)	ν(-COOH)
	ν_{asym}T-O	$\nu_{sym.}$T-O	T-O bend	D-R	Pore opening	ν_{sym}T-O	ν_{asym}T-O	water	(in-pane)		
SPAB	-	-	-	-	-	-	-	-	-	1600	1686
NaY	1032	720	463	576	390	787	1140	3456,1638			
Ni^{II}/Y	1030	723	460	576	386	789	1142	3400,3200,1635	1400		
Ni^{II}L/Y	1031	725	460	576	390	788	1145	3563,3276,1639	1400	1542	1510

Table 3 Some surface characteristics and lattice parameters of the different samples.

Sample	S_{BET} (m^2/g)	S_t (m^2/g)	$S_{(mic)}$ (m^2/g	$S_{(meso)}$ (m^2/g)	$S_{(ext)}$ (m^2/g	V_p (cm^3/g)	$V_{(mic)}$ (cm^3/g)	$V_{(mes)}$ (cm^3/g)	r (Å)	Cell constant (Å)*	Cell volume (Å)^3	Crystallinity %
NaY	902	758	225.7	676.3	89.7	0.80	0.59	0.21	22.21	24.64	14959	100
Ni^{II}/Y	783	804	189	593	31	0.69	0.54	0.15	22.17	24.56	14814	100
Ni^{II}L/Y	624	526	103	521	50	0.51	0.39	0.11	20.40	24.49	14695	98

Note: (S_{BET}) BET-surface area; (S_t) surface area derived from V_{1-t} plots; (S_{mic}) surface area of micropores; (S_{mes}) surface area of mesopores; (S_{ext}) external surface area; (V_p) total pore volume; (V_{mic}) pore volume of micropores; (V_{mes}) pore volume of mesopores; (r) mean pore radius.

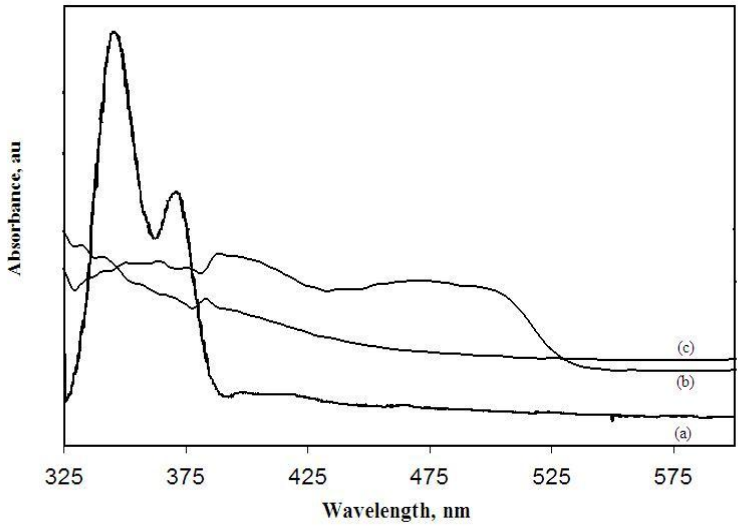

Fig. 1. UV–Vis diffuse reflectance spectra of (a) Ni^{II}/Y, (b) SBAP and (c) Ni^{II}L/Y.

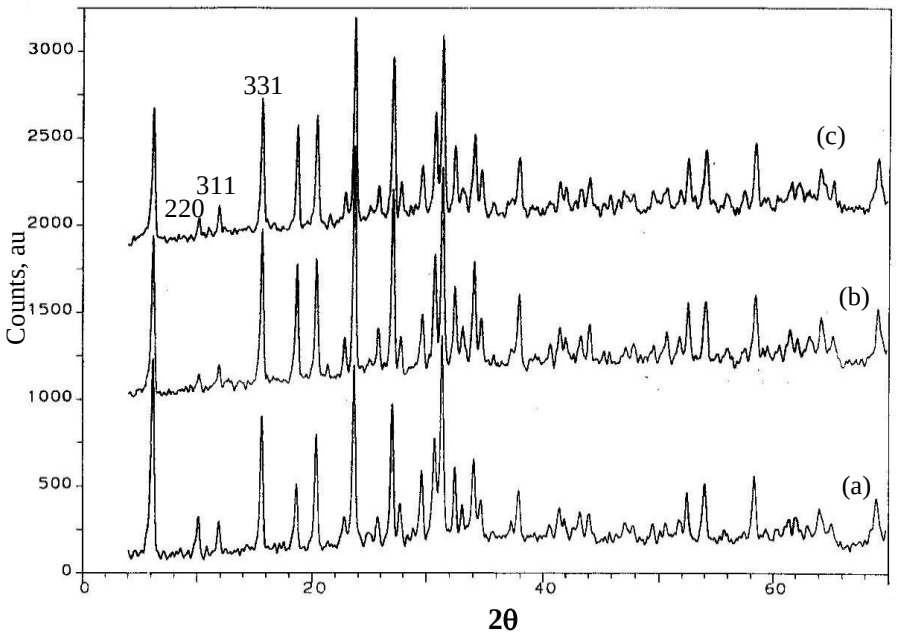

Fig. 2. X-ray powder diffraction patterns of (a) NaY, (b) Ni^{II}/Y and (c) Ni^{II}L/Y.

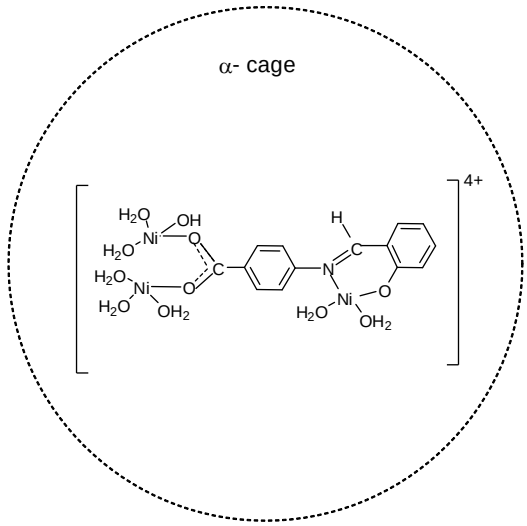

Fig. 3. Schematic diagram of $Ni^{II}L$ complex in zeolite Y.

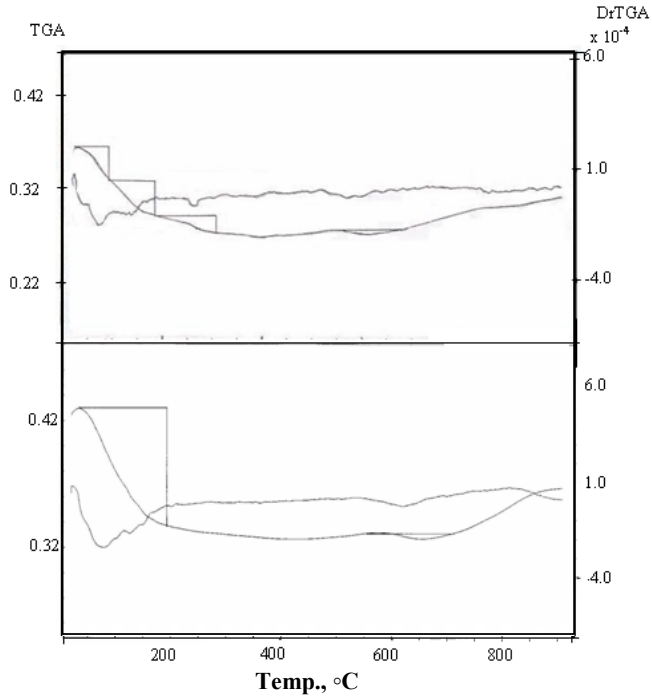

Fig. 4. TGA and DTG curves of Ni^{II}/Y (top), and Ni^{II}L/Y (bottom).

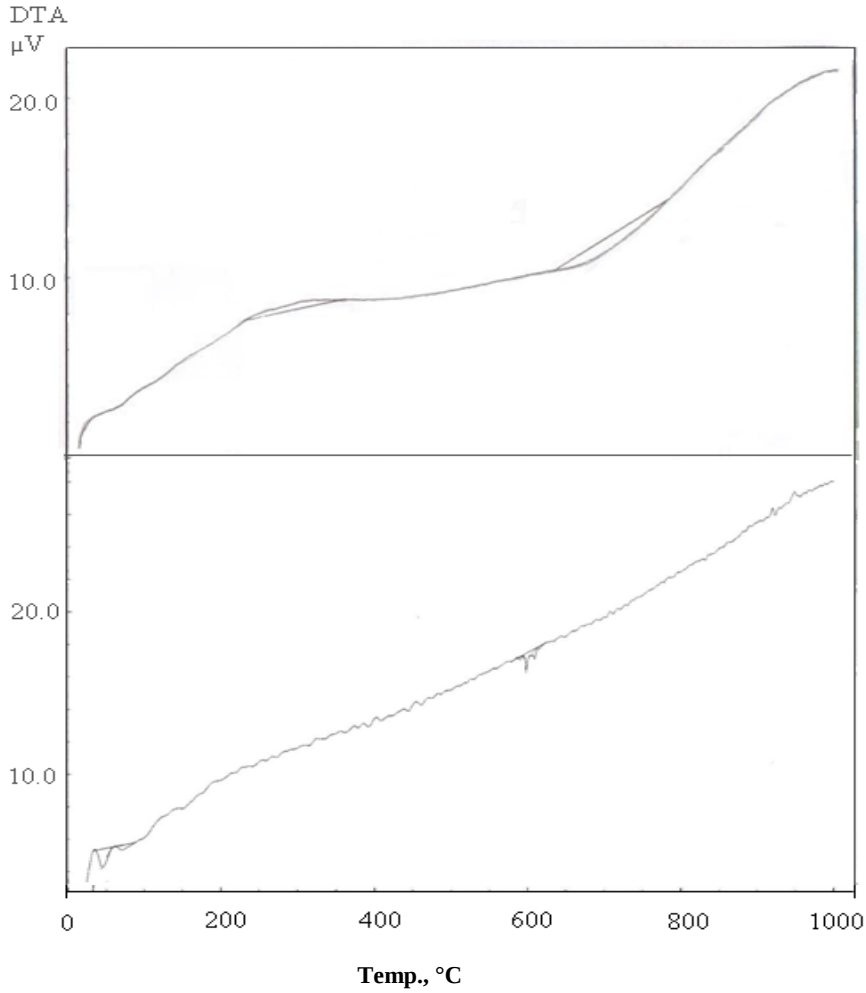

Fig. 5. DTA curves of Ni^{II}/Y (top), and Ni^{II}L/Y (bottom).

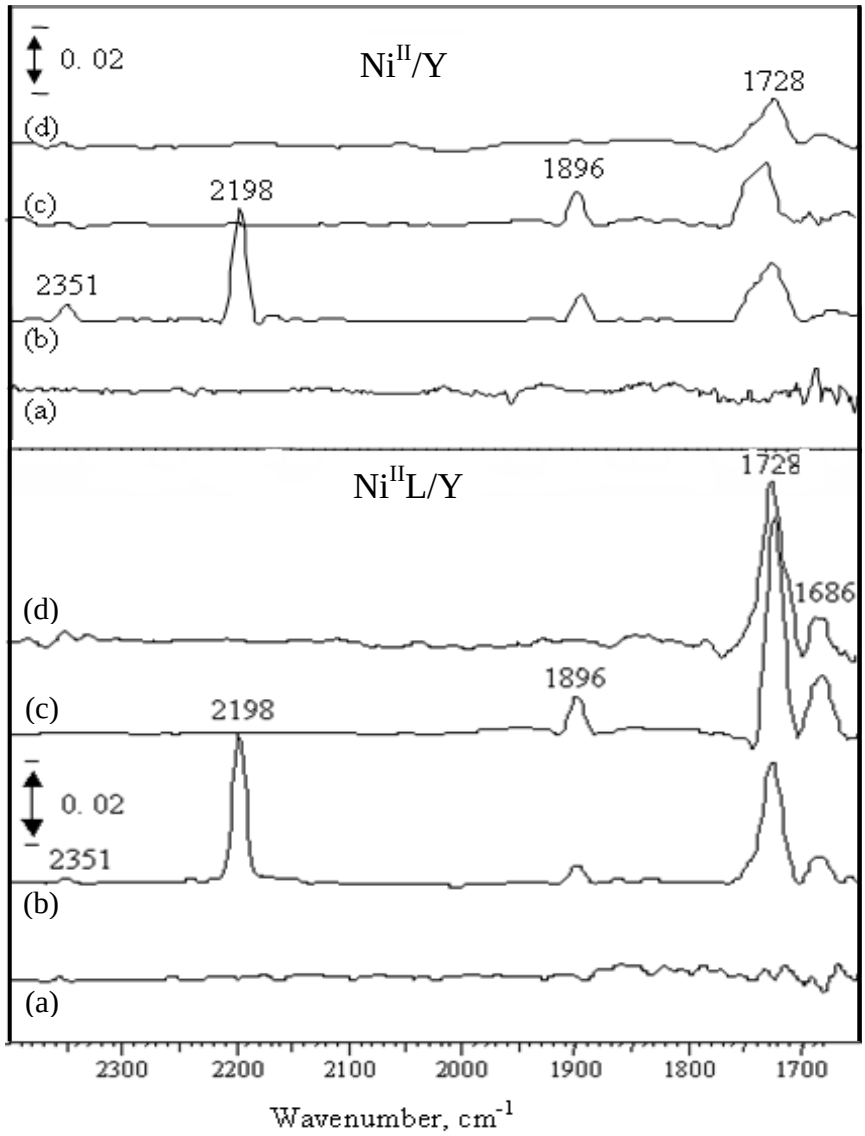

Fig. 6. ***In situ*** **FT-IR spectra of CO (50 Torr equilibrium pressure) adsorbed on Ni^{II}/Y and Ni^{II}L/Y at room temperature, after subtraction of CO-free spectrum; (a) solid evacuated at 300 °C, (b) at equilibrium gas phase, (c) after (b) evacuated at RT and (d) after (c) evacuated at 50 °C.**

References

1. D.W. BRECK, Zeolite Molecular Sieves: Structure, Chemistry and Use, John Wiley, New York, 1974.
2. H. VAN BEKKUM, E.M. FLANIGEN, J.C. Jansen, Introduction to Zeolite Science and Practice in Elsevier, Amsterdam, 1991.
3. K.O. XAVIER, J. Chacko, K.K. M. Yusuff, J. Mol. Catal. A Chem. 178 (2002) 275.
4. R. GANISAN, B. VISWANATHAN, J. Mol. Catal. A Chem. 181 (2002) 99.
5. N. HERRON, J. Coord. Chem. 19 (1988) 25.
6. E. L. CLENNAN, Coord. Chem. Rev. 248 (2004) 477.
7. D. BRUNEL, N. BELLOCQ, P. SUTRA, A. CAUVEL, M. LASPE´RAS, P. MOREAU, F. DI RENZO, A. GALARNEAU, F. FAJULA, Coord. Chem. Rev. 178–180 (1998) 1085.
8. C. BOWERS, P.K. DUTTA, J. Catal. 122 (1990) 271.
9. K.J. BALKUS JR., C.D. HARGIS, S. KOWALAK, ACS Symp. Ser. 499 (1992) 347.
10. G.A. OZIN, C. Gil, Chem. Rev. 89 (1989) 1749.
11. L.H. LUNSFORD, Rev. Inorg. Chem. 9 (1987) 1.
12. M. R. MAURYA, A. K. CHANDRAKAR, Sh. Chand, J. Mol. Catal. A: Chem. 274 (2007) 192.
13. S.M. FANG, J. PETUNCHI, J. LEGLISE, W.S. MILLMAN, W.K. Hall, J. Catal. 96 (1985) 182.
14. P.R. SHUKLA, V.K. SINGH AND A.M. JAISWAL, J. Indian chem. Soc., 60 (1987) 321.
15. M.G. BHOWON, H. LI. KAM WAH, R. Narain, Polyhedron 18 (1999) 341.
16. T.M. SALAMA, A. HUSSEN, Z.M. EL-BAHY, Micropor.Mesopor.Mater. 89 (2006) 251.
17. A.I. VOGEL, A Text Book of Quantitative Inorganic Analysis, Longmans, 5th Ed., London (1989).
18. M. FLANIGEN, Adv. Chem. Ser. 119 (1973) 121.
19. W.G. EWING, Instrumental Methods of chemical Analysis, 4th Ed. Mc Graw-Hill Koga-Kusha, 1975; A.I. Vogel, A Text Book of Practical Organic Chem., 3rd Ed., Longman, 1975.
20. M.M. BHADBHADE, D. Srinivas, Inorg. Chem. 32 (1993) 6122.
21. W.M. COLEMAN, L.T. Taylor, Inorg. Chem. 10 (1971) 2195.

22. D.J. PARRILLO, D. DOLENEC, R.J. GORTE AND R.W. MCCABE, J. Catal. 142 (1993) 708.
23. E.D. GARBOWSKI, C.J. Irodatas, Phys. Chem. 86 (1982) 97.
24. K.J. BALKUS, A. GABRIELOV, J. Inclusion Phenomena and Molecular Recognition in Chemistry 21 (1995) 159.
25. A.B.P. LEVER, Inorganic Electronic Spectroscopy, Elsevier, Amsterdam (1968).
26. T.M. SALAMA, T. SHIDO, R. OHNISHI, M. ICHIKAWA, J. Phys. Chem. 100 (1996) 3688.
27. W.H. QUAYLE, J.H. Lunsford, Inorg. Chem. 21 (1982) 2226.
28. M.N. BAE, M.K. SONG, Y. KIM, Bull. Kor. Chem. Soc. 22 (2001) 1081.
29. R. RAJA, P. Ratnasamy, J. Catal. 170 (1997) 244.
30. J. PERI, J. Catal. 86 (1984) 84.
31. C. HU, Y. CHEN, P. LI, H. MIN, Y. CHEN, A. Tian, J. Mol. Catal. A: Chem. 110 (1996) 163.
32. T. NAKATA, J. Chem, Phys. 26 (1) (1976) 487.
33. V. SANCHEZ ESCRIBANO, G. BUSCA, V. LORENZELLI, J. Phys. Chem. 95 (1991) 5541.
34. M.M. BADBHADE, D. SRINIVAS, Inorg. Chem. 32 (1993) 5458.